ELSEVIER

Contents lists available at ScienceDirect

#### Sensors and Actuators B: Chemical

journal homepage: www.elsevier.com/locate/snb



## Improving the sensitivity of electrochemical sensors through a complementary luminescent mode: A new spectroelectrochemical approach



Sayandev Chatterjee<sup>a,\*</sup>, Meghan S. Fujimoto<sup>a</sup>, Yu Hsuan Cheng<sup>b</sup>, Roli Kargupta<sup>b</sup>, Jennifer A. Soltis<sup>c</sup>, Radha Kishan Motkuri<sup>a</sup>, Sagnik Basuray<sup>b,\*</sup>

- <sup>a</sup> Energy and Environment Directorate, Pacific Northwest National Laboratory, Richland, Washington, 99352, United States
- b Department of Chemical, Biological and Pharmaceutical Engineering, New Jersey Institute of Technology, Newark, New Jersey, 07102, United States
- c Physical and Computational Science Directorate, Pacific Northwest National Laboratory, Richland, Washington, 99352, United States

#### ARTICLE INFO

# Keywords: Affinity sensors Luminescent sensors Sensitivity enhancement Limit of detection Rapid detection Spectroelectrochemistry

#### ABSTRACT

Rapid and sensitive detection and quantification of trace and ultra-trace analytes is critical to environmental remediation, analytical chemistry and defense from chemical and biological contaminants. Though affinity based electrochemical sensors have gained immense popularity, they frequently do not meet the requirements of desired sensitivity and detection limits. Here, we demonstrate a complementary luminescence mode that can significantly enhance sensitivity of impedance or voltammetric electrochemical sensors. Our methodology involves using a redox probe, whose luminescence properties change upon changing the oxidation state. By tailoring the system such that these luminescence changes can be correlated with the capture of target analytes, we are able to significantly lower the detection limit and improve the efficiency of detection compared to the electrochemical modes alone. Our proof-of-concept demonstration, using a model system designed for  $Ca^{2+}$  capture, illustrated that the luminescent mode allowed us to lower the limits of detection by three-orders of electrode design or cell configuration. Further, the linear ranges of detection are  $10^{-8}$  to  $10^{-3}$  M in the voltammetry mode,  $10^{-8}$  to  $10^{-8}$  to  $10^{-5}$  M in the impedance mode and  $2.5 \times 10^{-11}$  to  $10^{-7}$  M in the luminescent mode, providing a large range of operational flexibility.

#### 1. Introduction

Rapid, sensitive, *in-situ* detection and quantification of trace and ultratrace quantities of target analytes lies at the heart of environmental safety, nuclear forensics, chemical and biological defense and national security, as well as point-of-care applications [1]. In this regard, affinity-based sensors have gained immense popularity for the detection of both chemical and biological targets due to their ability to sense diverse classes of analytes, ranging from small molecules or ionic environmental contaminants to large proteins and biological entities [1–5]. These sensors are based on preferential recognition of the target analyte (s) of interest by a *capture-probe* immobilized on a platform, which results in their selective binding; this binding gives a unique response that can be measured using a variety of techniques: electrochemical, spectroscopic, magnetic and spectrometric.

Among these, electrochemical sensors have emerged as promising candidates for rapid, economic, highly selective and label-free detection of a diverse range of analytes ranging from chemical and environmental analytes to biological targets. These sensors can further be subdivided based on measurement conditions; the most popular ones being: (a) amperometric/coulometric, (b) voltammetric and (c) impedance sensors [1,6-8]. The former two involves measuring the current at the electrode as a function of the voltage applied across the electrolyte solution matrix and are measured in a direct current (DC) mode. In contrast, impedance sensors operate in alternating current (AC) mode and are based on measuring the changes in impedance at the electrode/ solution interface. Their working principle is the selective binding of the target analyte(s) of interest by a capture-probe immobilized on an electrode platform; this results in a marked increase in impedance of the platform-solution interface that is proportional to the target concentration. Analyte selectivity is imposed by the probes, which are tailored for very specific target binding. A key advantage of impedance sensors is that the sensing is not limited by the analyte class or type and depends solely on its ability to be uniquely recognized by the capture probe. This extends the applicability of this sensor to a wide range of substrates, the only requirement being the availability of an appropriate

E-mail addresses: Sayandev.Chatterjee@pnnl.gov (S. Chatterjee), sagnik.basuray@njit.edu (S. Basuray).

<sup>\*</sup> Corresponding author.

capture probe with tailored selectivity to specifically recognize the chosen target alone.

There are two modes of impedance measurements: non-Faradaic and Faradaic measurements. Typically non-Faradaic measurements are performed in the absence of any redox probe while Faradaic impedance measurements are performed in the presence of a redox probe [9]. The redox probe in Faradaic measurements is mostly present in the electrolyte solution in contact with the electrode [9], although instances have also been reported [10] where the probe has been incorporated in a thin-film polymer coated on the electrode surface to serve as an extension of the electrode In non-Faradaic measurements the interfacial capacitance at the electrode or modified electrode (electrode covered with thin film) surface is monitored for molecular modifications at the electrode [11]. In Faradaic measurements the charge transfer resistance at the electrode surface is monitored for changes in molecular modifications. An advantage of Faradaic mode lies in its ability to correlate the impedance changes at the electrode-electrolyte interface with the accompanying voltammetric response of the redox probe in solution, which allows tying the impedance mode with the voltammetric mode. This in fact can expand the applicability of the voltammetric mode of detection to species that are not themselves electroactive.

A key operative element for sensors in general and more specifically environmental sensors is sensitivity due to the need to detect trace or ultratrace quantities of contaminants. For electrochemical sensors, accepted approaches to enhance sensitivity and lower the limit of detection include (a) modifying electrode design and/or (b) analyte pretreatment (representative example being labeling in case of biomolecules).

One way of enhancing the sensitivity through modification of electrode design is to increase electrode surface area to increase the number of attached probes [1]. A few representative approaches to increase the surface area which have been adapted thus far include (a) self-assembled microcrystalline electrode monolayers with highly enhanced surface area [12,13],(b) depositing conducting polymers on the electrode surface that may also contain conducting elements such as Au [14] or Pt13] or carbon based materials [10,15] in order to extend the active electrode surface [16] or (c) using ultra-high surface area interdigitated electrodes [17,18]. Another approach is through reduction of the electrode size that allows for more sensitive detection [19].

An alternate approach involves modifying the target to enhance detection sensitivity; this involves prior label of the target before detection and is most relevant to bio-molecules. Labels include but are not limited to fluorophores [20], magnetic beads [21], enzymes with an easily detectable product [22,23], or any other options that can allow for facile target conjugation and convenient detection. However, labeling biomolecules can often change their parent properties including their binding and recognition, which alters their selectivity and therefore, effectiveness [24]. Further, this involves significant and comprehensive sample pretreatment steps which completely overrides the advantage of impedance mode as a rapid, in-situ sensing technique. Notable label-free alternatives include mechanical techniques such as quartz crystal microbalance (QCM) [25] and microcantilevers [26,27], surface plasmon resonance (SPR) [28,29], surface acoustic waves (SAW) [30,31], and field-effect transistors [32]; while these techniques add significant value to rapid, in-situ detection, their main disadvantage is the relatively small change in surface properties upon target binding, requiring sensitive readout methods [33].

We propose an alternative way of improving sensitivity by complementing the faradaic impedance mode with luminescence mode through a luminescent redox probe. Luminescent detection mode has independently been considered as a highly sensitive detection technique where, by proper selection of the luminescent probe, matrix interferences and autofluorescence effects can be largely eliminated [34–37]. In this regard, significant progress has been made in photoelectrochemical sensing which is based on photoinduced electron transfer processes at electrode/interfaces utilizing photoactive

electrode materials [38–43]. These sensors have captured significant interest in the field of analytical sensing due to their remarkable sensitivity, inherent miniaturization and ready integration in a wide variety of analytical fields [38,44–49]. However, their wide applicability is somewhat affected by the dual requirements of sophisticated fabrication methods as well as tedious coupling procedures required to improve reliability and minimize device-to-device variation [38,39].

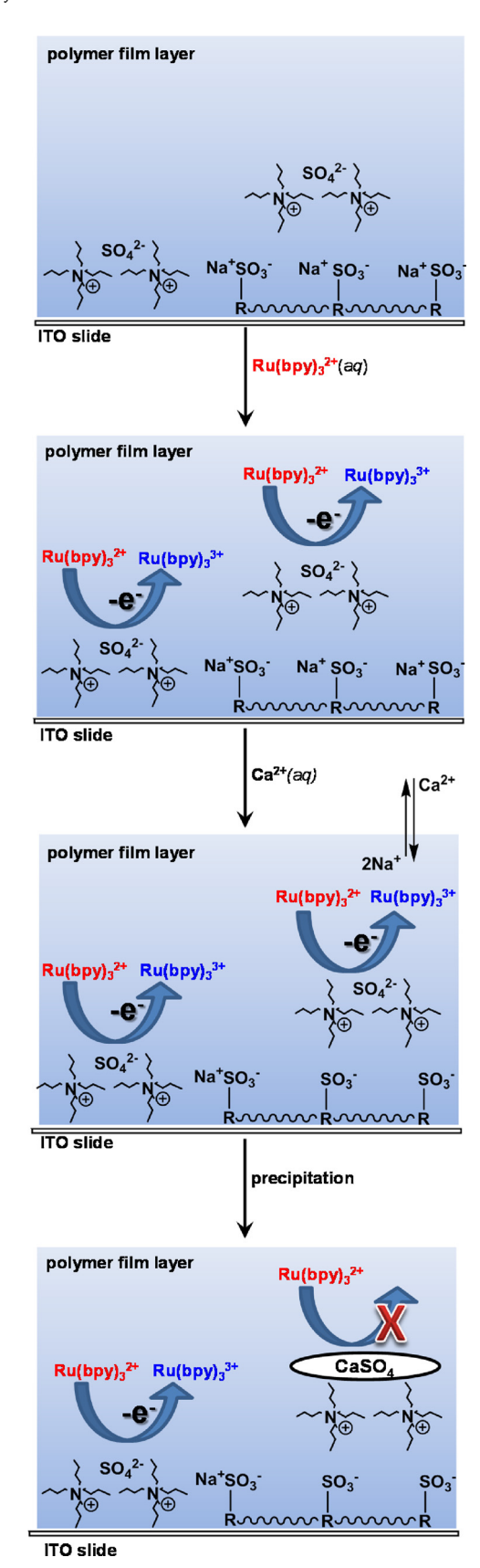
Our approach here involves a redox probe whose luminescence properties changes upon changing its oxidation state. As facile electron transfer takes place at the electrode-solution interface prior to analyte binding, the redox probe is readily converted from its non-luminescent to luminescent form. Subsequent binding of the target analyte on the capture probe impedes the electron transfer, inhibiting the conversion of the non-luminescent form to the luminescent form. This relative change in luminescence intensity can be effectively used for analyte detection and quantification. For ease of utilization of the luminescence mode, we plan on using optically transparent electrodes. Combining the impedance mode with a complementary luminescent mode can potentially enhance the limit of detection, without the need for elaborate and expensive target alteration or extensive device fabrication. However, to our knowledge this mode has not been adequately explored in the Faradaic impedance mode taking advantage of the luminescent properties of the redox probe in solution.

Our cumulative working strategy proposes a new spectroelectrochemical approach for analyte detection. Over the last several decades, spectroelectrochemistry has been a key analytical technique for detection and characterization of diverse analyte classes [50,51] that range across inorganic [52–56], organic [57,58], biological [59] and even radiological analytes [34,35,60,61]. However, most of the adapted spectroelectrochemical techniques are limited by the requirement of some characteristic spectroscopic and electrochemical property of the analyte that can be monitored. An additional advantage of our approach is that it judiciously makes use of a luminescent redox probe and therefore does not require the analyte itself to possess any unique spectroscopic or redox signatures, and therefore expands the applicability of the spectroelectrochemistry technique.

For proof-of-concept demonstration, we chose  ${\rm Ca}^{2^+}$  cations as our target of interest. We would like to emphasize here that the primary objective of this work is proof-of-concept demonstration of enhancement of sensitivity through the incorporation of the secondary luminescence detection mode. Selective target detection is not the goal of this work, and therefore the sensor capture probe is not expected to be unique to  ${\rm Ca}^{2^+}$  detection (unlike works on selective  ${\rm Ca}^{2^+}$  detection that include efforts by Arunkumar et al. [62] or by Singh et al. [63] to name a few) and will be responsive to other rare-earth cations as well. However, it is worth mentioning that a practical application of this sensor can be as a water hardness sensor.

Strategy: Our working strategy is based on selective capture of the target analyte by a capture-probe immobilized on an electrode platform, which will impede the mass transport of a chosen redox probe to the electrode. (Scheme 1) This impedance will affect the luminescence generated by electrochemical activation of the redox probe. For proofof-concept demonstration, we chose Ca<sup>2+</sup> cations as our target analyte. The capture probe comprises of an anionic polymer thin film composite preconcentrated with  $SO_4^{2-}$  anions (Scheme 1); this composite is layered on a working electrode surface. Upon Ca<sup>2+</sup> exposure, the electrostatic attraction between the anionic film and the dicationic target allows the cations to diffuse into the film. Once inside, Ca<sup>2+</sup> can readily react with the preloaded  $SO_4^{\,2-}$ , resulting in CaSO<sub>4</sub> precipitation within the film. The precipitate blocks the approach of a chosen redox probe to the electrode surface, leading to a reduction in current intensity of redox probe-voltammograms proportional to the Ca<sup>2+</sup> concentration.

To demonstrate the enhancement in sensitivity of the electrochemical response due to the incorporation of a secondary luminescent detection mode, [Ru(bpy)<sub>3</sub>]Cl<sub>2</sub>·6H<sub>2</sub>O is chosen as the redox probe. This



Scheme 1. Schematic representation of Ca<sup>2+</sup> detection.

choice is largely motivated by the redox properties of the compound, and in particular its varying luminescent behavior associated with the changes in its redox state.  $[Ru(bpy)_3]^{3+/2+}$  exhibits a chemically and

electrochemically reversible redox couple in aqueous solutions  $(E^{o^{\epsilon}}=1.27\ V\ vs.\ SCE)\ [50,64]$ , of which the reduced  $[Ru(bpy)_3]^{2^+}$  form shows a strong luminescence at 620 nm ( $\lambda_{ex}=532\ nm$ ) [65] while the oxidized  $[Ru(bpy)_3]^{3^+}$  form is non-luminescent under similar excitations [37]. Further, both the oxidized and reduced forms are sufficiently stable both chemically and electrochemically, unlike some other redox active luminescent probes such as  $[Re(dmpe)_3]^{2^+/^+}$  that are prone to air oxidation [66,67].

The  $[Ru(bpy)_3]^{3+/2+}$  will be embedded within the polymer film matrix. When the target  $Ca^{2+}$  analyte is absent in the test solution, the electroactive platform is conductive and can readily interconvert between the luminescent and non-luminescent forms. When  $Ca^{2+}$  is present in the solution, it can readily diffuse in the film and react with  $SO_4^{2-}$  anion to form a precipitate of  $CaSO_4$ , which will impede the mass transport of  $[Ru(bpy)_3]^{3+/2+}$  to the electrode, suppressing the interconversion between the luminescent and non-luminescent forms.  $Ca^{2+}$  detection and quantification can be done through a proportional change of either the electrochemical signal (voltammetric current or impedance) or the luminescent signal. Since the luminescence mode is expected to be more sensitive compared to the electrochemical mode, it can in principle allow us to attain lower detection limits.

Optically transparent Indium Tin Oxide (ITO) will be used as the electrode platform for the ease of utilization of the luminescence mode. Tetrabutylammonium sulfate is chosen as the  ${\rm SO_4}^{2-}$  anion source due to its miscibility with organic polymer electrolytes. Nafion is chosen as our polymer of choice over other anionic polymer polyelectrolytes (representative examples being SSEBS, PSS) based on the better affinity for and ease of incorporation of  $[Ru(bpy)_3]^{3+/2+}$  within Nafion films, [37,68,69], coupled within the extensive usage of Nafion on ITO based modified electrodes, [70,71], as well as the reported chemoluminescent behavior of  $[Ru(bpy)_3]^{3+/2+}$  within Nafion films. [69,70], The improved incorporation of  $[Ru(bpy)_3]^{3+/2+}$  within Nafion compared to SSEBS or PSS is related to the non-cross-linked nature of the former. This can be explained by the Gibbs-Donnan equation which predicts the thermodynamic behavior and distribution of charged particles across a semi-permeable membrane. [68,72], In cross-linked polymers, the cross-linking introduces a PV term which impedes migration of large ions (such as  $[Ru(bpy)_3]^{3+/2+}$ ). The absence of cross linkages in Nafion eliminates such discriminations, allowing their partitioning without any thermodynamic penalties. [68,73], Additional benefits of Nafion include its chemical stability to resist degradation under ambient environmental conditions and its well behaved electrochemistry in the common electrolytes and buffer solutions within the ITO potential window of -1.0 to +1.4 V vs Ag/AgCl; this allows us to make effective use of the electrochemical modulation of optical signal [37,74].

#### 2. Experimental section

#### 2.1. Reagents and materials

All chemical reagents were used without further purification. Nafion (average MW 1,100, 5 wt % solution in lower aliphatic alcohols and water; Fig. 1A), tetrabutylammonium sulfate (TBAS) solution (50 wt. % in H<sub>2</sub>O; Fig. 1B), 3-aminopropyltriethoxy silane (APTS; Fig. 1C) and *tris*-(2,2′-bipyridyl)ruthenium(II) dichloride hexahydrate ([Ru(bpy)<sub>3</sub>]Cl<sub>2</sub>·6H<sub>2</sub>O) were all purchased from Sigma-Aldrich. Calcium nitrate (Ca(NO<sub>3</sub>)<sub>2</sub>) was obtained from Fisher Scientific. All solutions were prepared using deionized water (D2798 Nanopure water purification system, Barnstead, Boston, MA) in a 0.1 M KNO<sub>3</sub> supporting electrolyte solution. Indium tin oxide (ITO)-coated 1737 F glass pieces (~135 nm thick ITO layer, 11–50  $\Omega$ /cm [2]; hereafter termed substrates) were obtained from Thin Film Devices.

A 
$$Na^+SO_3^ Na^+SO_3^-$$

$$F_2C$$

$$F_2$$

$$F_2$$

$$F_2C$$

$$F_2$$

$$F_3$$

$$F_4$$

$$F_2$$

$$F_2$$

$$F_3$$

$$F_4$$

$$F_2$$

$$F_3$$

$$F_4$$

$$F_4$$

$$F_2$$

$$F_3$$

$$F_4$$

$$F_4$$

$$F_4$$

$$F_5$$

$$F_5$$

$$F_5$$

$$F_7$$

$$F_8$$

Fig. 1. Structural formulae of the components of the polymer film: (A) Nafion, (B) tetrabutylammonium sulfate and (C) the bifunctional linker 3-aminopropyl-triethoxy silane (APTS).

#### 2.2. Electrochemical measurements

For voltammetric experiments, a standard three-electrode configuration was used with an Epsilon potentiostat, while electrical impedance spectroscopy (EIS) measurements were performed on a Gamry 600 potentiostat/galvanostat. All voltammetric scans were recorded employing a  $10 \times 40 \, \text{mm}$  ITO-glass transparent working electrode, a platinum auxiliary electrode, and an Ag/AgCl reference electrode (3 M NaCl, BAS). Peak currents (*ip*) for CV and DPV were estimated with respect to the extrapolated baseline current as described by Kissinger and Heineman [60,75]. EIS data fitting was carried out using Z-view software.

#### 2.3. Luminescence measurements

Luminescence spectra were acquired using either an Acton Instruments-based or an Ocean Optics-based system. The Acton Research InSpectrum 150 with controlling Spectrasense software was equipped with a back-thinned, cooled charge coupled device (CCD) camera and fiber-optic input. Excitation was performed using a 532 nm diode-pumped solid-state (DPSS) laser (Melles Griot, 20 mW CW). A 532 nm holographic notch filter (Kaiser) was used to reduce laser light back scattered into the InSpectrum 150 spectrometer. Signal integration times were typically 500 ms using a 2 mm slit width for a 600 g/mm grating blazed at 500 nm. Step-index silica-on-silica optical fibers were purchased from Romack, Inc. The Ocean Optics system consisted of a USB-200FL spectrometer and Ocean Optics 00IBase32 Spectroscopy Software.

#### 2.4. Luminescence measurements under stationary voltage

All luminescence measurements under stationary voltage were performed in a custom made cell previously reported in our earlier work [35], and has been described in detail the supporting information section S1.

#### 2.5. Ion chromatography measurements

Anions were analyzed quantitatively using either a Dionex Reagent Free Ion Chromatography System 5000 (RFICS-5000) with an AS-AP auto-sampler or a Dionex Reagent Free Ion Chromatography System 2000 (RFICS-2000) with an AS-1 auto-sampler. Both instruments were calibrated using a multi-component anion solution made by Inorganic

Ventures. The calibrated range was 0.01 ppm to 7.5 ppm. The calibration was verified immediately with an Initial Calibration Verification (ICV) standard and during sample analysis with a Continuing Calibration Verification (CCV) standard run every ten samples at a minimum. A Continuing Calibration Blank (CCB) was analyzed after each CCV to ensure background signals and potential carryover effects were not a factor. The CCV standard was prepared from a multi-component anion solution made by SPEX CertiPrep. All calibration verification values were ensured to be within  $\pm$  10% of the target concentrations to comply with the QA/QC requirements as defined in the Hanford Analytical Quality Assurance Requirements Document (HASQARD\*), Volumes 1 and 4. The solutions were measured as received without dilution. The detection limit for  $\mathrm{SO_4}^{2-}$  in this method was 1.5 mM.

#### 2.6. Thin-Film preparations

ITO-coated glass substrates were thoroughly cleaned with soap, rinsed with ethanol and deionized water, and argon-plasma cleaned for about 30 min prior to coating. A Harrick Scientific plasma cleaner was used for final cleaning of substrates and electrodes. Following this, the glass substrates were functionalized with the bifunctional linker APTS (vide supra). The APTS polymer was added to prevent the dissolution of Nafion film in water over time, as it had been observed that the bifunctional APTS layer significantly improved the life-time and preserved the integrity of films in contact with aqueous solutions. For this procedure, clean substrates were soaked overnight in 2 M NaOH in order to activate the surface. After rinsing with water, the substrates were soaked in 5% APTS in acetate buffer, pH 5.5, at 90 °C for 5 h. The substrates were then rinsed with deionized water, spun dry for 30 s, and immediately used for film coating. A spin-coater (model 1 p.m.101DT-R485 Photo-Resist Spinner, Headway Research, Inc.) was used for preparation of films of required thicknesses. The stock solution of Nafion was diluted to 1% using 2-propanol and blended with 0.5 wt % tetrabutylammonium sulfate solution also diluted using 2-propanol. A 50 µL aliquot of the blended solution was pipetted onto the substrates, which were spun at a preoptimized speed (3000 rpm) for 30 s [35]. The variation of film thickness, at constant concentration of Nafion, had been optimized previously for spin speed and spin time [76]. Our obtained film thickness (measured with ellipsometry) was 250  $\pm$  10 nm (1% solution) on ITO substrates, and was desired based on observations of films with similar thickness resulting in a linear response [37]. The film-coated substrates were left overnight to further cure at ambient

temperature. For electrochemical experiments, a 1 cm portion of one end of the ITO substrate was masked with tape before spin coating. The area free of film was then used for electrical contact with the electrode.

Ellipsometric measurements (film optical constants and thicknesses) were made using a J.A.Woollam, Inc., variable-angle spectroscopic ellipsometer (vertical configuration). This instrument was equipped with an adjustable retarder (AutoRetarder) that enabled measurements of  $\psi$  and  $\Delta$  over the full angular range (0–90 and 0–360 degrees, respectively). The instrument also permitted depolarization of the light to be measured. Woollam WVASE32 software was used for optical modeling.

Subsequently, the coated ITO electrodes were kept immersed in water for three days for the hydration of the film. This was followed by immersing the film in a solution of Ru(bpy) $_3$ Cl $_2$  in aqueous 0.1 M KNO $_3$  for a given period to preconcentrate the film before its usage. For studies of voltammetric behavior of  $[Ru(bpy)_3]^{3^{+/2+}}$  couple in the composite film, the films were each exposed to a solution of 0.1 mM  $[Ru(bpy)_3]^{2^+}$  for 30 min. For studies of Ca $^{2^+}$  detection using the composite films, the films were exposed to a solution of 0.5 mM  $[Ru(bpy)_3]^{2^+}$  for 1 day. To determine the leaching of SO $_4^{2^-}$  from the prepared thin films into the aqueous solutions, ion chromatography studies were conducted on the contacted solutions, and no detectable leaching of SO $_4^{2^-}$  was observed suggesting the combination of Nafion, TBAS and APTS helps in arresting the leaching.

For detection purposes, stock solutions with varying  $\text{Ca}^{2+}$  concentrations were obtained by dissolving appropriate amounts of Ca  $(\text{NO}_3)_3$  in DI water. The independent ITO slides coated each with the Nafion-TBAS composite and preloaded with  $\text{Ru}(\text{bpy})_3\text{Cl}_2$  were separately exposed to these solutions with varying  $\text{Ca}^{2+}$  concentrations for 30 min each, and the exposure was monitored using tandem electrochemistry and luminescence measurements in a custom-made cell previously reported elsewhere as shown in supporting information (Figure S1; section S1).

#### 2.7. Transmission electron microscopy measurements

To characterize the chemical identity of the precipitate formed upon Ca<sup>2+</sup> exposure, transmission electron microscopy (TEM) measurements were conducted. After prolonged exposure of the Nafion-TBAS composite film loaded on an ITO slide to a solution of Ca<sup>2+</sup>, the film was scrapped off, suspended in water to dissolve the Nafion. A specimen was prepared for transmission electron microscopy by sonicating the suspended solids in water for three minutes prior to placing a single drop on a 200 mesh copper TEM grid coated with holey carbon film (Electron Microscopy Supplies) and allowing to dry. The drop was pipetted from the upper portion of the supernatant to maximize the

likelihood of capturing particles that were thin enough for TEM and electron diffraction, rather than those large enough to settle due to gravity. The grid was imaged in an FEI Tecnai T20 TEM (Thermo Fisher Scientific) equipped with a field emission gun and operating at 200 keV in bright field and diffraction modes. Image capture was performed on an FEI Eagle charge capture device (CCD) camera using TIA software (Thermo Fisher Scientific).

Measurements for indexing diffraction patterns were performed in FIJI (ImageJ) v1.51i. (ImageJ is a public domain image processing and analysis program written by Wayne S. Rasband at the National Institutes of Health, Bethesda, MD, U.S.A.) [77,78] Patterns were compared with crystal structures for gypsum (CaSO<sub>4</sub>·2H<sub>2</sub>O), bassanite (CaSO<sub>4</sub>·0.5H<sub>2</sub>O), and anhydrite (CaSO<sub>4</sub>) retrieved from the American Mineralogist Crystal Structure Database (gypsum AMCSD ID: 0,011,093; bassanite AMCSD ID: 0,006,909; anhydrite AMCSD ID: R040061).

#### 3. Results

### 3.1. Electrochemical and luminescent behavior of $[Ru(bpy)_3]^{3+/2+}$ within the Nafion/TBAS composite film

The electrochemical behavior of [Ru(bpy)<sub>3</sub>]<sup>3+/2+</sup> have been studied before both in aqueous solutions as well within Nafion films, using an ITO electrode. However, to our knowledge, the behavior has not been studied within a Nafion/TBAS composite film. For the preparation of the Nafion/TBAS composite film loaded with [Ru(bpy)<sub>3</sub>]<sup>2+</sup>, the prepared film was allowed to soak in a 0.1 M NaNO<sub>3</sub> solution for 3 days to hydrate the film. Subsequently, the film was allowed to dry. This was followed by immersing the film in a solution containing  $100\,\mu\text{M}$  Ru  $(bpy)_3^{2+}$  aqueous solution for 30 min. This immersion resulted in electrostatic absorption of Ru(bpy)<sub>3</sub><sup>2+</sup> into the film as reflected by development of an orange-red coloration of the film as well as the clear redox peaks of [Ru(bpy)<sub>3</sub>]<sup>3+/2+</sup> observed in subsequent voltammetry experiments on the loaded film. For voltammetry experiments, the [Ru  $(bpy)_3]^{2+}$  loaded film was immersed in an aqueous solution of 0.1 M NaNO<sub>3</sub>, and the working electrode potential was scanned between 0.0 V and +1.6 V (vs. Ag/AgCl) of which the region between +0.6 V and +1.6 V is shown in Fig. 2 (left panel). A range of scan rates varying from 10 mV/s to 1000 mV/s were used in this study.

The well-defined voltammograms show a chemically reversible Ru  $(bpy)_3^{3+/2+}$  redox couple similar to that observed previously for other Nafion solutions (voltammograms shown in Figure S2 (left panel)) [79]. The voltammetric profiles are comparable to that observed by Bertoncello, Unwin and coworkers on  $[Ru(bpy)_3]^{2+}$  systems loaded into

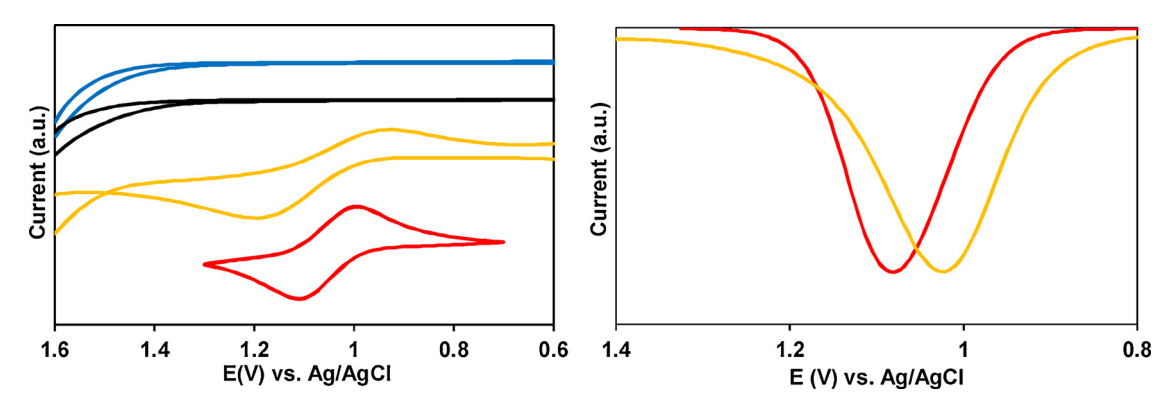
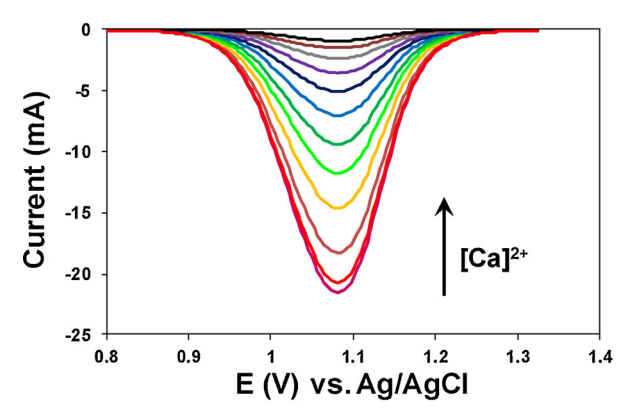
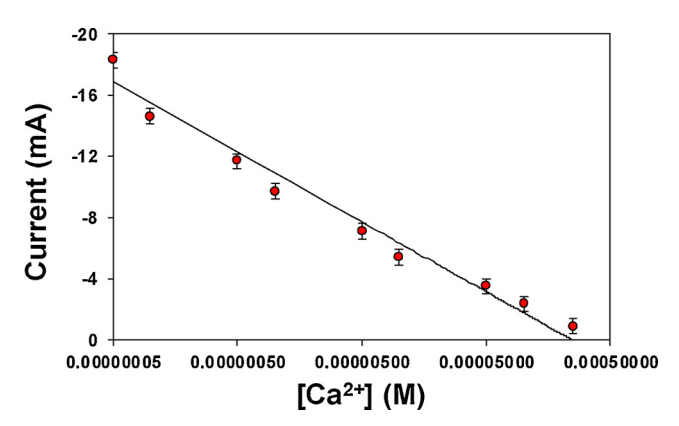


Fig. 2. (left) Cyclic voltammograms at  $\nu=100~{\rm mVs^{-1}}$  of (top blue line) 0.1 M aqueous KNO<sub>3</sub> using ITO electrode, (second from top black line) 0.1 M aqueous KNO<sub>3</sub> using Nafion-TBAS composite film on an ITO working electrode, (second from bottom yellow line) 0.1 mM Ru(bpy)<sub>3</sub><sup>3+/2+</sup> in 0.1 M aqueous KNO<sub>3</sub> using ITO electrode, (bottom red line) Nafion-TBAS composite film on an ITO working electrode exposed to 0.1 mM [Ru(bpy)<sub>3</sub>]<sup>3+/2+</sup> for 30 min (right) Differential pulse voltammograms of (orange line) 0.1 mM [Ru(bpy)<sub>3</sub>]<sup>3+/2+</sup> in 0.1 M aqueous KNO<sub>3</sub> using ITO electrode, (red line) Nafion-TBAS composite film on an ITO working electrode exposed to 0.1 mM [Ru(bpy)<sub>3</sub>]<sup>3+/2+</sup> for 30 min. The peak currents are normalized for comparison. (For interpretation of the references to colour in this figure legend, the reader is referred to the web version of this article).





**Fig. 3.** (left) Differential pulse voltammograms on Nafion-TBAS composite film on an ITO working electrode exposed to  $0.5\,\mathrm{mM}$  [Ru(bpy)<sub>3</sub>]<sup>3+/2+</sup> for 1 day, with progressively increasing Ca<sup>2+</sup> concentrations: (\_\_) 0 M Ca<sup>2+</sup>, (\_\_) 1 × 10<sup>-8</sup> M Ca<sup>2+</sup>, (\_\_) 5 × 10<sup>-8</sup> M Ca<sup>2+</sup>, (\_\_) 1 × 10<sup>-7</sup> M Ca<sup>2+</sup>, (\_\_) 1 × 10<sup>-7</sup> M Ca<sup>2+</sup>, (\_\_) 1 × 10<sup>-8</sup> M C

Nafion using graphitic electrodes [80–82]. The difference between the anodic and cathodic peak potential ( $\Delta E_{\rm p}$ ) was ca. 120 mV at  $\nu = 100 \, {\rm mV s}^{-1}$  ( $E_{\rm pa} = 1.11 \, {\rm V}$ ;  $E_{\rm pa} = 0.99 \, {\rm V}$ ). As the scan rates were increased,  $E_{pc}$  values were shifted to more negative potentials while  $E_{pa}$ potentials moved to more positive values, resulting in an increase in the magnitude of  $\Delta E_{\rm p}$  to 150 mV at  $\nu = 500$  mV s<sup>-1</sup> and 180 mV at  $\nu = 1000 \,\mathrm{mV \ s^{-1}}$ . Similarly, lowering the scan rate resulted in decreasing  $\Delta E_{\rm p}$ , with the  $E_{\rm pa}$  and  $E_{\rm pc}$  moving closer to each other so that  $\Delta E_{\rm p}=70\,{\rm mV}$  at  $\nu=10\,{\rm mV}$  s<sup>-1</sup>. In all cases, the values of  $(E_{\rm pa}+E_{\rm pc})$  /  $2 = E_{1/2}$  were nearly constant at +1.05 V, and independent of the scan rate. A plot of the anodic and cathodic peak current vs (scan rate)<sup>1/2</sup> within the film shown in Figure S2 (right panel) demonstrates good adherence to linearity confirms that diffusion is predominantly semiinfinite, rather than restricted (i.e., thin layer) for this thickness of polymer film and this range of scan rates. This is in keeping with the Randles-Sevcik equation which states that the peak current,  $i_p$ , is proportional to the square root of the scan rate,  $(\nu)^{1/2}$  (Eq. (1)) for a semiinfinite diffusion controlled system [83].

$$i_p = (2.69 \times 10^5) n^{3/2} A D^{1/2} C^0 v^{1/2}$$
(1)

In fact, this behavior illustrates a difference in our electrochemical behavior in the Nafion-TBAS composite compared to that observed by Bertoncello, Unwin and coworkers on just Nafion. While our results indicate semi-infinite diffusion controlled system for the entire range of scan rates studied, the work by Bertoncello, Unwin and coworkers suggest a thin-layer behavior at slow scan rates (< 100 mV/s) and diffusion controlled behavior at faster scan rated (100-500 mV/s) [84]. The reason for this may be the choice of a significantly thicker film ( $\sim$ 250 nm) in our work compared to the previous work ( $\sim$  17 nm). It is also worth noting that the properties of our Nafion-TBAS composite may be significantly different from pure Nafion, which may also influence the observed redox behavior. In spite of this, the peak to peak separation of the [Ru(bpy)<sub>3</sub>]<sup>3+/2+</sup> redox couple when preconcentrated in Nafion-TBAS films is observed to be lower than that for the couple in aqueous solution for the same scan rate. This is presumably an effect of diffusion; for Ru(bpy)<sub>3</sub><sup>2+</sup> species preloaded within the film that is in vicinity of the electrode surface, heterogeneous electron transfer kinetics between the redox probe and electrode is presumably less diffusion limited than compared to another that has to migrate all the way from somewhere in the bulk solution. This leads to the former being a more electrochemically reversible process compared to the latter.

The DPV of  $[Ru(bpy)_3]^{3+/2+}$  on the ITO electrode in neutral medium shows a well-defined anodic wave (yellow trace in Fig. 2, right panel) at 1.03 V vs. Ag/AgCl, assigned to the oxidation of  $[Ru(bpy)_3]^{2+}$ . On the other hand, the DPV of  $[Ru(bpy)_3]^{3+/2+}$ 

preconcentrated in Nafion-TBAS film shows a much narrower peak, albeit shifted to slightly more positive potentials of 1.08 V vs. Ag/AgCl (red trace in Fig. 2, right panel). The narrowing of the peak is again a consequence of diffusion.

#### 3.2. Detection of Ca2+

 ${\rm Ca}^{2+}$  detection and quantification were determined independently using three different modes: (1) the voltammetric mode, (2) the EIS mode and (3) the luminescent mode. For studies of  ${\rm Ca}^{2+}$  detection using the composite films, the films loaded onto the ITO surface were exposed to a solution of 0.5 mM  ${\rm [Ru(bpy)_3]}^{2+}$  for 1 day prior to detection by voltammetric, EIS or luminescence mode.

#### 3.2.1. Voltammetric mode

The electrochemical response of the probe upon exposure to Ca<sup>2+</sup> ions was quantified by measuring the magnitude of the peak current of the  $[Ru(bpy)_3]^{2+}/[Ru(bpy)_3]^{3+}$  redox process within the film using differential pulse voltammetry. The peak current observed in the absence of Ca2+ gives the maximum peak current intensity. It was observed that upon exposure to higher and higher concentrations of Ca<sup>2+</sup>, the voltammograms showed a progressive decrease in the peak current  $[Ru(bpy)_3]^{2+} \rightarrow [Ru(bpy)_3]^{3+}$ magnitude during (Fig. 3(left)). A plot of peak current versus the logarithm of Ca<sup>2+</sup> concentration shows a linear relation, all other factors remaining constant. However, for low  ${\rm Ca}^{2+}$  concentrations below 10 nM, the electrochemical mode is not able to effectively discern it for the given electrochemical configuration. From the plot of peak currents of the DPV for  $0.5 \,\mathrm{mM} \, [\mathrm{Ru}(\mathrm{bpy})_3]^{3+/2+}$  versus the logarithm of the aqueous Ca<sup>2+</sup> concentration (Fig. 3 (right), the non-logarithmic plot is shown in Figure S3), a preliminary value of the limit of detection (LOD) can be calculated based on the IUPAC recommended formula [2] as reported by Long et al. [85].

$$DL = \frac{k \cdot S_b}{m} \tag{2}$$

Here, DL is the detection limit, k is a numerical constant, m is the slope of the linear region of the plot, and  $S_b$  is the standard error for the blank measurements, respectively. In accord with IUPAC recommendations, a k value of 3 was applied, which corresponds to a 99.87% confidence level. A detection limit of 7.5 nM is determined for aqueous  $Ca^{2+}$  using the above formulae on the voltammetric data.

#### 3.2.2. EIS mode

The electrochemical impedance response of the probe upon exposure to Ca<sup>2+</sup> ions was quantified by fitting the resultant EIS responses

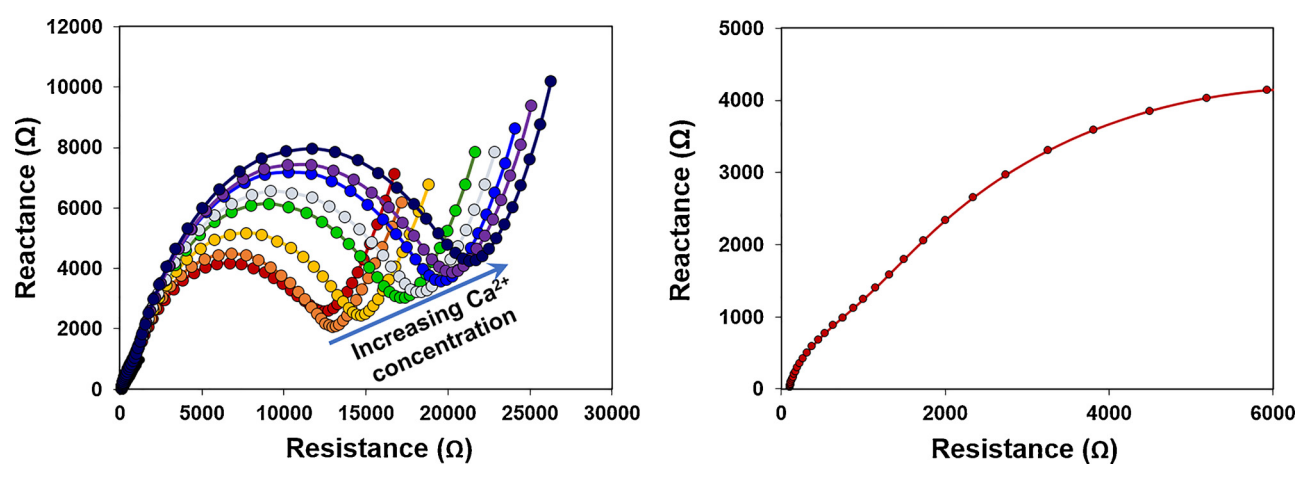


Fig. 4. (left) Nyquist plots showing the EIS response of ITO electrode modified with Nafion-TBAS with increasing  $Ca^{2+}$  concentrations in the range of  $1.0 \times 10^{-8}$  M  $\cdot 1 \times 10^{-5}$  M: (red symbols and trace) Nafion-TBAS modified electrode with no  $Ca^{2+}$ , (orange symbols and trace) 10 nM  $Ca^{2+}$ , (yellow symbols and trace) 50 nM  $Ca^{2+}$ , (green symbols and trace) 10 nM  $Ca^{2+}$ , (violet symbols and trace) 50 nM  $Ca^{2+}$ , (royal blue symbols and trace) 10 µM  $Ca^{2+}$ , (violet symbols and trace) 50 µM  $Ca^{2+}$ , (Navy blue symbols and trace) 10 µM  $Ca^{2+}$ . (black symbols and trace = the bare ITO electrode). (right) Magnified EIS response from the ITO electrode modified with Nafion-TBAS composite film showing two semi-circles and hence two interfaces, namely the ITO bare electrode and the Nafion-TBAS composite film modified electrode. (For interpretation of the references to colour in this figure legend, the reader is referred to the web version of this article).

to an equivalent circuit. It is worthwhile to note that as the measurements were performed in the presence of the redox probe [Ru  $(bpy)_3]^{2^+}/[Ru(bpy)_3]^{3^+}$ , the change in the interfacial resistance at the electrode surface (Faradaic EIS) was used here to quantify the  $Ca^{2^+}$  ions. To interpret EIS into relevant physical processes, it is critical to describe an equivalent circuit that has an equivalent impedance similar to that observed from experiments. An equivalent circuit can be composed of a multitude of resistances and capacitances, like a parallel combination of capacitance and resistance or series combination of capacitance and resistances [86]. The equivalent circuit that fits the impedance of the experiments is described in detail below.

It is critical to recognize here that there are two interfaces, the electrode-electrolyte interface and the modified electrode/Nafion-TBAS composite film-electrolyte interface. This is clearly shown in Fig. 4 (right). For the bare electrode the simple Randle's circuit can be used to fit the impedance date (Figs. 4 and 5 A). It consists of an active solution resistance  $R_{\rm S}$  in series with the parallel combination of the double-layer capacitance  $C_{\rm dl}$  and a faradaic resistance  $R_{\rm CT}$  [86]. Here a constant phase element (CPE) is used in place of the double layer capacity ( $C_{\rm dl}$ ) due to the inherent roughness of the electrode [11]. The solution resistance  $R_{\rm S}$  is a representation of the conductivity of the electrolyte and any resistance in the wires used to measure EIS. At the electrode interface, there are multiple paths for the ions in the solution. The ions can either collect near the interface as a charge storage mechanism, or

they can react (Faradic Reaction) with the electrolytes. The storing of charge at the electrode solution interface is called the Electrical Double Layer or the Debye Layer and is designated as  $C_{\rm dl}$  in the equivalent circuit [87]. The faradic resistor is represented as the charge-transfer resistance  $R_{\rm CT}$ . The Faradic resistor often leads to a depletion of ions at the interface. This results in the formation of a diffusive gradient from the bulk to the interface. This is represented as the Warburg Element,  $W_{\rm D}$ , in the circuit. At higher frequencies, the Warburg impedance tends to be smaller since reactants are not allowed to have enough time to diffuse, while at lower frequencies, the reactants get adequate time to diffuse leading to an increase in the Warburg impedance [88]. As the diffusive gradients are anisotropic due to the roughness of the electrode, the Warburg impedance is also modeled as a CPE [88].

Post modification of the electrode with the polymer film, the EIS circuit is modified as shown in Fig. 5B. Here one notices two semicircles due to the two interfaces that have appeared (Fig. 4). It is worthwhile to note that as the film is porous, the EIS response should come from both the electrode and polymer film modified electrode. The polymer film will increase the resistance of the Faradaic current of the  $[Ru(bpy)_3]^{2+/3+}$  redox species. As the electrolyte does not change, the double layer capacitance associated with the electrode or the modified electrode should be similar. Hence the relaxation frequency ( $\sim 1/RC$ ) time of the modified electrode will be significantly lower than the electrode. This is evident from Fig. 4 (right panel) wherein the EIS response from the

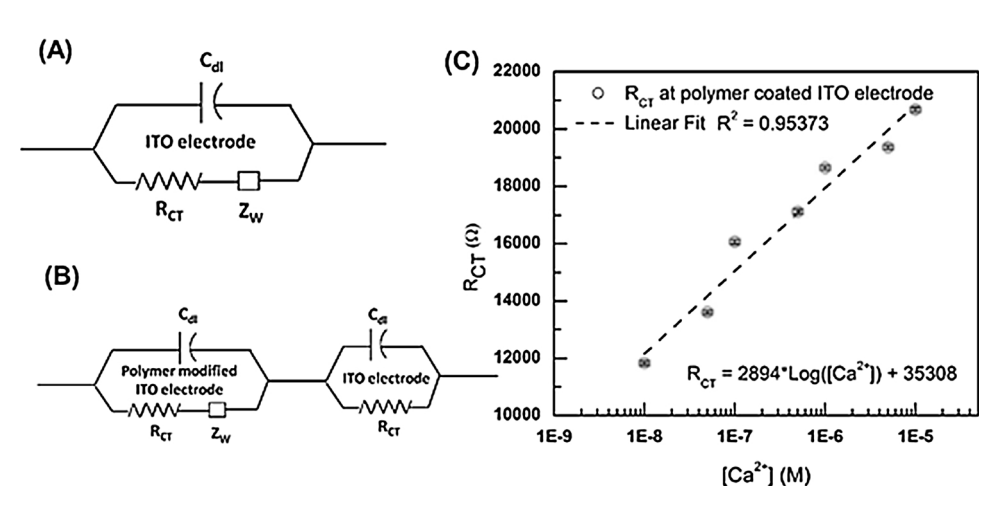


**Fig. 5.** (A) Equivalent circuit for bare ITO electrode. (B) The equivalent circuit for ITO electrode modified with polymer film. (C)  $R_{CT}$  values from Nafion-TBAS composite film modified ITO electrode as a function of increasing  $Ca^{2+}$  concentrations in the concentration range of  $1.0 \times 10^{-8}$  M -  $1 \times 10^{-5}$  M. The equation of the line: Charge Transfer Resistance ( $R_{CT}$ ,  $\Omega$ ) = 2894 log [ $Ca^{2+}$ ] + 35,308.

Table 1
The fitted data values are shown from fitting the EIS response from Fig. 4 to the appropriate circuits in Fig. 5A and B. (NA = not applicable).

	ITO Electrode Circuit Parameters			Nafion-TBAS composite film modified electrode Circuit Parameters	
	R <sub>S</sub> (Ω)	C <sub>dl</sub> (Capacitance) (F)	C <sub>dl</sub> (Phase)	C <sub>dl</sub> (Capacitance) (F)	C <sub>dl</sub> (Phase)
Bare Electrode Nafion-TBAS film electrode	95.79 ± 0.24 96.07 ± 0.90	$3.45 \pm 0.16 *10^{-6}$ $5.7 \pm 1.44 *10^{-7}$	0.838 ± 0.005 0.877 ± 0.049	NA 1.19 ± 0.14 *10 <sup>-6</sup>	NA 0.817 ± 0.015

modified film electrode appears later. Thus, the Warburg response (diffusion at low frequency) is now associated with the modified film electrode (circuit in Fig. 5B) rather than with the electrode response (as in Fig. 5A).

Post data fitting (fits shown in Figure S4), Table 1 tabulates the average response of R<sub>S</sub>, C<sub>dl</sub> (modified and bare electrode) and W<sub>D</sub>. The value of the solution resistance or R<sub>S</sub> does not change between the two circuits as expected. Further C<sub>dl</sub> which is modeled as a constant phase element has almost the same capacitance value at the electrode for both the circuit models and nearly the same at the modified film electrode. The exponent is close to 1, which signifies that the response is mostly capacitive. As is expected from a Faradaic impedance-based study, the value of the charge transfer resistance, R<sub>CT</sub> changes from the bare electrode to the modified electrode film. However, this increase is more significant at the modified film electrode rather than at the bare electrode in the circuit in Fig. 5B. It is worthwhile to note that as expected the magnitude of R<sub>CT</sub> does not change at the electrode whether it is the bare ITO, or the modified polymer film coated ITO. As expected, R<sub>CT</sub> at the polymer film coated ITO interface is significantly larger than at the ITO interface due to the increased resistance to the Faradaic current from [Ru(bpy)<sub>3</sub>]<sup>2+</sup>. A plot of charge transfer resistance, R<sub>CT</sub>, at the polymer film coated ITO electrode with increasing Ca<sup>2+</sup> concentrations follows a linearly increasing trend for Ca<sup>2+</sup> concentration as shown in Fig. 4 and 5C. R<sub>CT</sub> progressively increases with increasing Ca<sup>2+</sup> addition as the Ca<sup>2+</sup> ions migrate into the film and react with the SO<sub>4</sub><sup>2-</sup> ions to form insoluble CaSO<sub>4</sub>. This precipitation progressively retards the electron transfer from the electrode, and proportionally blocks lowering of the [Ru(bpy)<sub>3</sub>]<sup>2+</sup>. Using the circuit model in Fig. 5B to the EIS data of the Nafion-TBAS composite film gives us the background  $R_{CT}$  of 11,662  $\Omega.$  The  $R_{CT}$  from the plot of the charge transfer resistance for  $0.5 \, \text{mM} \, [\text{Ru(bpy)}_3]^{3\,+/2\,+}$  versus the logarithm of the aqueous  $\text{Ca}^{2\,+}$ concentration (Fig. 5C) must be greater than this value to be measurable which gives a LOD of 6.75 nM.

#### 3.2.3. Luminescence mode

An alternate mode involved monitoring the luminescence response of the [Ru(bpy)<sub>3</sub>]<sup>2+/3+</sup> preloaded in the electrode polymer film, and how it was impacted by progressive Ca<sup>2+</sup> addition. One advantage of using the complementary luminescent mode for analytical purposes is to be able to access the comparatively more sensitive changes in luminescent response for effective quantification of the analyte.34, 54 In this mode, the working electrode potential was fixed at a stationary voltage of 1.1 V vs. Ag/AgCl where, in the absence of any other perturbations of the electrochemical system, the entire Ru population is expected to exist in the non-luminescent  $[Ru(bpy)_3]^{3+}$  form. In the absence of Ca<sup>2+</sup>, no luminescence is observed from the electrode film, suggesting quantitative oxidation of the  $[Ru(bpy)_3]^{2+}$  to  $[Ru(bpy)_3]^{3+}$ under the highly oxidizing stationary voltage. However, upon progressive Ca<sup>2+</sup> addition, it is observed that the luminescence intensity progressively increases (Fig. 6 (left panel)). This is because, with the addition of more and more Ca2+ ions, they migrate into the film and react with the  $SO_4^{\ 2^-}$  ions to form insoluble CaSO<sub>4</sub>. This precipitation progressively retards the electron transfer from the electrode, and proportionally blocks lowering of the [Ru(bpy)<sub>3</sub>]<sup>2+</sup> luminescence intensity by preventing its oxidation to [Ru(bpy)<sub>3</sub>]<sup>3+</sup>.

As with the electrochemical mode, the limit of detection can also be

obtained from a slight modification of the procedure used elsewhere using luminescence intensity values.  $^{35-36}$  A plot of the luminescent intensities of the Ru(bpy) $_3^{2^+}$  (measured at 620 nm upon excitation with  $\lambda_{ex}=532$  nm) with increasing Ca $^{2^+}$  concentrations initially follows a linear trend for Ca $^{2^+}$  concentrations within  $2.5\times10^{-11}$  M  $_2$  10 $^{-7}$  M as shown in Fig. 6 (right panel). Beyond Ca $^{2^+}$  concentrations greater than  $10^{-7}$  M, a break in the linearity is observed. This can presumably be a consequence of the effect of saturation resulting in levelling off of the luminescence intensity. From the initial linear region, a detection limit of 7.5 pM is determined for aqueous Ca $^{2^+}$ .

A comparison of the above results suggests that *the luminescent mode lowers the limit of detection by 3-orders of magnitude compared to both the voltammetric and the EIS mode*, and therefore can be tailored to enhance sensitivity, all other parameters and conditions remaining constant.

#### 3.3. Characterization of the precipitate by TEM

Transmission electron microscopy images show particles ca. 500 nm to  $5\,\mu m$  in the longest dimension. This represents the size fraction that was suspended into water when the precipitate was sonicated and was small enough to image with TEM, and does not exclude the presence of larger particles. Analysis of electron diffraction patterns show the presence of the calcium sulfate minerals gypsum and bassanite. Fig. 7 shows transmission electron micrographs and corresponding electron diffraction patterns of gypsum particles. This confirms the production of calcium sulfate as gypsum during the experiments. Bassanite may also be a product, as shown in electron micrographs and diffraction patterns in Fig. 8. The presence of bassanite may also be the result of the dehydration of particles (loss of 1.5 H<sub>2</sub>O per formula unit compared to gypsum) due to electron beam exposure. Some particle damage was observed during the imaging process, mostly in the form of  $10-30\,\mathrm{nm}$ circular voids, but not all bassanite particles display this damage. None of the diffraction patterns were found to match the fully dehydrated calcium sulfate phase anhydrite. These observations prove the formation of calcium sulfate during the detection process.

#### 3.4. Effects of other cations

As mentioned earlier, the capture probe in our sensor configuration is expected to respond to all metal ions that get entrapped in the film and form a precipitate with  $SO_4{}^{2-}$  ions, that can block the mass transport of  $Ru(bpy)_3{}^{3+/2+}$  to the electrode. To test the effects of exposure to other divalent cations, the probe was separately exposed to 10 nM solution of  $Sr^{2+}$ ,  $Ba^{2+}$  and  $Pb^{2+}$ . It was observed that  $Ba^{2+}$  generated the most significant increase in impedance, followed by  $Pb^{2+}$ , which was followed by  $Pb^{2+}$  and  $Pb^{2+}$ , as shown in Fig. 9 (left panel). This may presumably be a consequence of the respective solubility products of these cations  $(K_{sp}, Ca^{2+}, 2.4 \times 10^{-4}; Sr^{2+}, 3.5 \times 10^{-7}; Pb^{2+}, 1.6 \times 10^{-8}; Ba^{2+}, 1.1 \times 10^{-10})$ . In fact, the respective  $R_{CT}$  values are observed to follow an inverse linear relationship with the logarithm of the respective solubility products of the  $Pb^{2+}$  salts  $Pb^{2+}$  and  $Pb^{2+}$  an

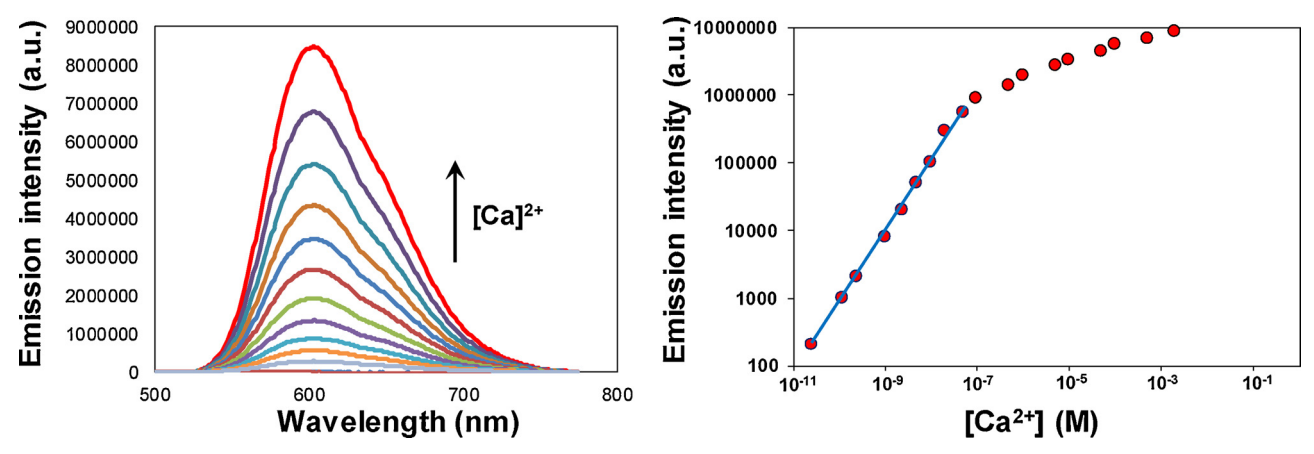


Fig. 6. (left) Emission profiles of  $0.5\,\mathrm{mM}$  [Ru(bpy)<sub>3</sub>]<sup>3+/2+</sup> loaded Nafion-TBAS composite film on an ITO working electrode under a stationary potential of 1 V, upon exposure to progressively increasing Ca<sup>2+</sup> concentrations. Select profiles are shown with Ca<sup>2+</sup> concentrations of (\_\_)  $0\,\mathrm{M}$  Ca<sup>2+</sup>, (\_\_)  $1\,\times\,10^{-8}\,\mathrm{M}$  Ca<sup>2+</sup>, (\_\_)  $5\,\times\,10^{-8}\,\mathrm{M}$  Ca<sup>2+</sup>, (\_\_)  $1\,\times\,10^{-8}\,\mathrm{M}$  Ca<sup>2+</sup>, (\_\_)  $5\,\times\,10^{-8}\,\mathrm{M}$  Ca<sup>2+</sup>, (\_\_)  $5\,\times\,10^{-6}\,\mathrm{M}$  Ca<sup>2+</sup>, (\_\_) 5

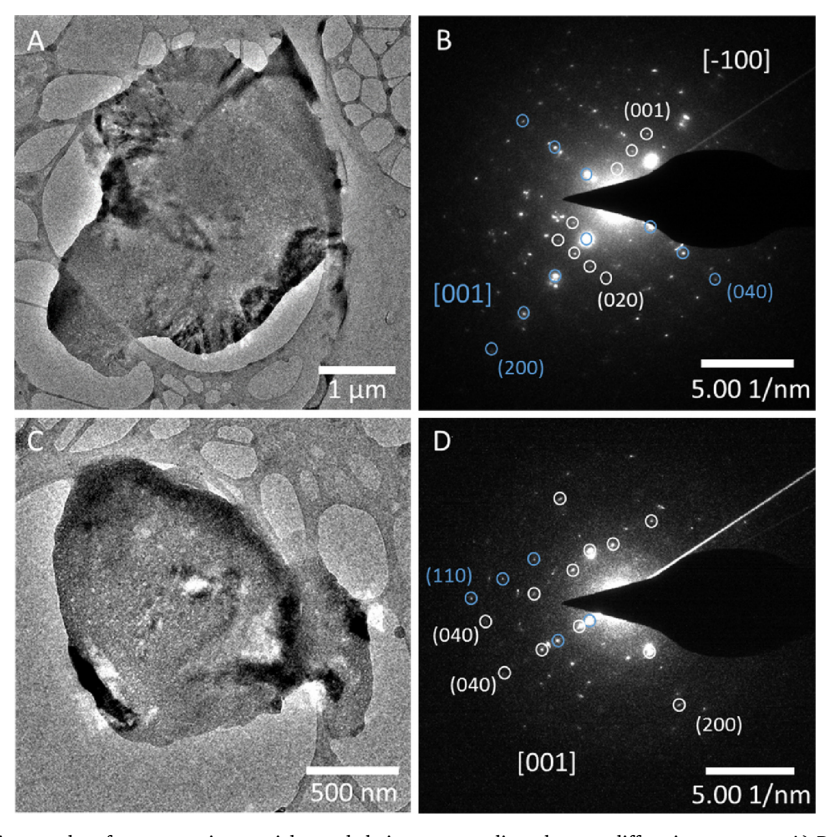


Fig. 7. Transmission electron micrographs of gypsum microparticles and their corresponding electron diffraction patterns. A) Polycrystalline microparticle with crystal domains oriented along [001] and  $\bar{1}$ 00] and B) electron diffraction pattern. C) Polycrystalline microparticle with one component oriented along [001] and D) electron diffraction pattern. Diffraction spots with spacing corresponding to (110) were also identified and do not match the appropriate interplanar angles to be part of the domain with the [001] zone axis.

#### 4. Discussion and conclusions

The strategic design of the capture probe involved tetrabutylammonium sulfate (TBAS) as the  ${\rm SO_4}^{2-}$  source embedded within the Nafion film. The lipophilicity of TBAS and its miscibility with Nafion prevented its loss into the aqueous layer.  ${\rm Ru(bpy)_3}^{2+}$  was preloaded into the film taking advantage of the dicationic nature of Ru  ${\rm (bpy)_3}^{2+}$  and the non-cross linking within Nafion. In the absence of  ${\rm Ca}^{2+}$ ,  ${\rm [Ru(bpy)_3]}^{3+/2+}$  interconversion occurred readily within the

film which was monitored electrochemically as well as by luminescence spectroscopy.

Upon exposure to aqueous  $Ca^{2+}$ , the  $Ca^{2+}$  ions were observed to readily diffuse into the film due to electrostatic attraction between the anionic film and the dications, presumably substituting the  $Na^+$  ions rather than the more lipophilic  $Bu_4N^+$  ions. Once inside the film, the  $Ca^{2+}$  ions reacted with the preloaded  $SO_4^{2-}$ , resulting in the precipitation of  $CaSO_4$  within the film, as verified using electron diffraction. The  $CaSO_4$  precipitate blocked the heterogeneous electron transfer

Fig. 8. Transmission electron micrograph and electron diffraction pattern of bassanite microparticle oriented along the [131] zone axis.

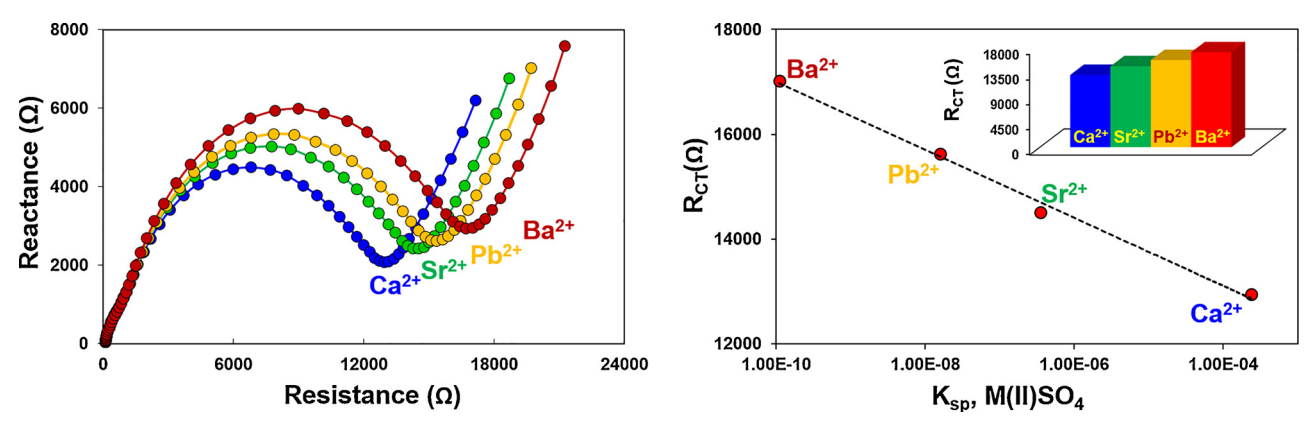


**Fig. 9.** (left) Nyquist plots showing the EIS response of ITO electrode modified with Nafion-TBAS with upon exposure to 10 nM M(II) ions: (blue symbols and trace)  $Ca^{2+}$  ions, (green symbols and trace)  $Sr^{2+}$  ions, (yellow symbols and trace)  $Pb^{2+}$  ions, (red symbols and trace)  $Ba^{2+}$  ions. (right) Semi logarithmic plot of  $R_{CT}$  values obtained from the respective Nyquist plots upon exposure of the composite film to 10 nM of various M(II) cations versus the solubility product of the corresponding M (II)SO<sub>4</sub> (M(II) =  $Ca^{2+}$ ,  $Sr^{2+}$ ,  $Pb^{2+}$ ,  $Ba^{2+}$ ). Inset:  $R_{CT}$  values for the four cations. (For interpretation of the references to colour in this figure legend, the reader is referred to the web version of this article).

from the ITO electrode to the film, impeding  $[Ru(bpy)_3]^{3^+/2^+}$  interconversion. The total amount of  $Ca^{2^+}$  could be quantified directly from the proportional decrease in the peak current for the  $[Ru(bpy)_3]^{3^+/2^+}$  voltammetric process in the DPV experiments, or from the progressive build-up of the  $R_{CT}$  values with increasing  $Ca^{2^+}$  concentrations in the EIS experiments. Alternatively, quantification using the differential luminescence of  $[Ru(bpy)_3]^{3^+/2^+}$  lowered the limit of detection by **three orders of magnitude** compared to the two electrochemical modes. This demonstrates that our approach can serve the dual objective of (a) combining impedance mode with a complementary luminescent mode that improves the accuracy of quantification, and (b) enhances the limit of detection without requiring elaborate and expensive target alteration or extensive device fabrication. Further, the linear ranges of detection are  $10^{-8}$ - $10^{-3}$  M in the voltammetry mode,  $10^{-8}$ - $10^{-5}$  M in the impedance mode and  $2.5 \times 10^{-11}$ - $10^{-7}$  M in the luminescent mode, providing a large range of operational flexibility.

We would like to reiterate here that this work serves merely as a proof-of-concept demonstration of the technique alone where a secondary luminescence mode can be used to lower the detection limit. While this validates the ability of the luminescence mode, it is not meant to serve as a real sensor for selective  ${\rm Ca}^{2+}$  detection as it will not differentiate between alkaline earth metals or other metals that form a precipitate with  ${\rm SO_4}^{2-}$  (as observed with  ${\rm Ba}^{2+}$ ,  ${\rm Sr}^{2+}$  and  ${\rm Pb}^{2+}$ ). However, the sensor can be tailored for monitoring the hardness of water. Future work will involve using judiciously tailored nanoporous probes (representative examples being metal organic frameworks [89,90]) to enhance target selectivity.

#### Conflicts of interest

The authors declare no conflicts of interest.

#### Acknowledgments

This research was supported by (1) the Laboratory Directed Research and Development Program at the Pacific Northwest National Laboratory (SEED EED) (S.C.) and (2) a National Science Foundation (NSF) Career grant(#1751759), "ASSURED electrochemical platform for multiplexed detection of Cancer Biomarker Panel using Shear-Enhanced Nanoporous-Capacitive Electrodes" (S.B.). Pacific Northwest National Laboratory (PNNL) is operated by Battelle for the U.S. Department of Energy under Contract DE-AC05-76RL01830. We would like to especially acknowledge Dr. Tatiana Levitskaia for helpful discussions. Part of this research was performed at Environmental Molecular Sciences Laboratory, a national scientific user facility at PNNL managed by the Department of Energy's Office of Biological and Environmental Research.

#### Appendix A. Supplementary data

Supplementary material related to this article can be found, in the online version, at doi:https://doi.org/10.1016/j.snb.2018.10.093.

#### References

[1] J.S. Daniels, N. Pourmand, Label-free impedance biosensors; opportunities and

- challenges, Electroanalysis 19 (12) (2007) 1239-1257.
- [2] R. Ballerstadt, A. Kholodnykh, C. Evans, A. Boretsky, M. Motamedi, A. Gowda, R. McNichols, Affinity-based turbidity sensor for glucose monitoring by optical coherence tomography: toward the development of an implantable sensor, Anal. Chem. 79 (18) (2007) 6965–6974.
- [3] A.P.F. Turner, Biochemistry biosensors sense and sensitivity, Science 290 (5495) (2000) 1315–1317.
- [4] Y.B. Zhu, Y.F. Hao, E.A. Adogla, J. Yan, D.C. Li, K.X. Xu, Q. Wang, J. Honea, Q. Lin, A graphene-based affinity nanosensor for detection of low-charge and low-molecular-weight molecules, Nanoscale 8 (11) (2016) 5815–5819.
- [5] W.W. Zhao, J.J. Xu, H.Y. Chen, Photoelectrochemical bioanalysis: the state of the art, Chem. Soc. Rev. 44 (3) (2015) 729–741.
- [6] D.R. Thevenot, K. Toth, R.A. Durst, G.S. Wilson, Electrochemical biosensors: recommended definitions and classification, Biosens. Bioelectron. 16 (1-2) (2001) 121–131
- [7] T.G. Drummond, M.G. Hill, J.K. Barton, Electrochemical DNA sensors, Nat. Biotechnol 21 (10) (2003) 1192–1199.
- [8] E. Bakker, Electrochemical sensors, Anal. Chem. 76 (12) (2004) 3285-3298.
- [9] X.F. Guo, A. Kulkarni, A. Doepke, H.B. Halsall, S. Iyer, W.R. Heineman, Carbohydrate-based label-Free detection of Escherichia coli ORN 178 using electrochemical impedance spectroscopy, Anal. Chem. 84 (1) (2012) 241–246.
- [10] D.L. Zhao, T.T. Wang, D. Han, C. Rusinek, A.J. Steckl, W.R. Heineman, Electrospun carbon nanofiber modified electrodes for stripping voltammetry, Anal. Chem. 87 (18) (2015) 9315–9321.
- [11] K. Eugenii, W. Itamar, Probing biomolecular interactions at conductive and semiconductive surfaces by impedance spectroscopy: routes to impedimetric immunosensors, dna-sensors, and enzyme biosensors, Electroanalysis 15 (11) (2003) 913–947.
- [12] C.Z. Li, Y.L. Liu, J.H.T. Luong, Impedance sensing of DNA binding drugs using gold substrates modified with gold nanoparticles, Anal. Chem. 77 (2) (2005) 478–485.
- [13] M.S. Desilva, Y. Zhang, P.J. Hesketh, G.J. Maclay, S.M. Gendel, J.R. Stetter, Impedance based sensing of the specific binding reaction between Staphylococcus enterotoxin-B and its antibody on an ultra-thin platinum film, Biosens. Bioelectron. 10 (8) (1995) 675–682.
- [14] S.Q. Hu, Z.M. Xie, C.X. Lei, G.L. Shen, R.Q. Yu, The integration of gold nanoparticles with semi-conductive oligomer layer for development of capacitive immunosensor, Sens. Actuat B-Chem. 106 (2) (2005) 641–647.
- [15] T.T. Wang, D.L. Zhao, X.F. Guo, J. Correa, B.L. Riehl, W.R. Heineman, Carbon nanotube-loaded nafion film electrochemical sensor for metal ions: europium, Anal. Chem. 86 (9) (2014) 4354–4361.
- [16] S. Cosnier, Affinity biosensors based on electropolymerized films, Electroanalysis 17 (19) (2005) 1701–1715.
- [17] W. Laureyn, D. Nelis, P. Van Gerwen, K. Baert, L. Hermans, R. Magnee, J.J. Pireaux, G. Maes, Nanoscaled interdigitated titanium electrodes for impedimetric biosensing, Sens. Actuat B-Chem. 68 (1-3) (2000) 360–370.
- [18] T.C. Hang, A. Guiseppi-Elie, Frequency dependent and surface characterization of DNA immobilization and hybridization, Biosens. Bioelectron. 19 (11) (2004) 1537–1548
- [19] D. Friedrich, C. Please, T. Melvin, Optimisation of analyte transport in integrated microfluidic affinity sensors for the quantification of low levels of analyte, Sens. Actuat B-Chem. 131 (1) (2008) 323–332.
- [20] I.L. Medintz, H.T. Uyeda, E.R. Goldman, H. Mattoussi, Quantum dot bioconjugates for imaging, labelling and sensing, Nat. Mater. 4 (6) (2005) 435–446.
- [21] I.M. Hsing, Y. Xu, W.T. Zhao, Micro- and nano-magnetic particles for applications in biosensing, Electroanalysis 19 (7-8) (2007) 755–768.
- [22] S. Nuber, U. Zabel, K. Lorenz, A. Nuber, G. Milligan, A.B. Tobin, M.J. Lohse, C. Hoffmann, Beta-arrestin biosensors reveal a rapid, receptor-dependent activation/deactivation cycle, Nature 531 (7596) (2016) 661.
- [23] J. Deen, C. Vranken, V. Leen, R.K. Neely, K.P.F. Janssen, J. Hofkens, Methyltransferase-directed labeling of biomolecules and its applications, Angew Chem. Int. Ed. 56 (19) (2017) 5182–5200.
- [24] B.B. Haab, Methods and applications of antibody microarrays in cancer research, Proteomics 3 (11) (2003) 2116–2122.
- [25] C.K. O'Sullivan, G.G. Guilbault, Commercial quartz crystal microbalances theory and applications, Biosens. Bioelectron. 14 (8-9) (1999) 663–670.
- [26] N. Backmann, C. Zahnd, F. Huber, A. Bietsch, A. Pluckthun, H.P. Lang, H.J. Guntherodt, M. Hegner, C. Gerber, A label-free immunosensor array using single-chain antibody fragments, Proc. Natl. Acad. Sci. U. S. A. 102 (41) (2005) 14587–14592.
- [27] C. Ziegler, Cantilever-based biosensors, Anal. Bioanal. Chem. 379 (7-8) (2004) 946–959.
- [28] H.H. Nguyen, J. Park, S. Kang, M. Kim, Surface plasmon resonance: A versatile technique for biosensor applications, Sensors-Basel 15 (5) (2015) 10481–10510.
- [29] L.A. Garcon, M. Genua, Y.J. Hou, A. Buhot, R. Calemczuk, T. Livache, M. Billon, C. Le Narvor, D. Bonnaffe, H. Lortat-Jacob, Y. Hou, A versatile electronic Tongue based on surface plasmon resonance imaging and Cross-reactive sensor arrays-A mini-review, Sensors-Basel 17 (5) (2017).
- [30] G. Destgeer, B.H. Ha, J. Park, J.H. Jung, A. Alazzam, H.J. Sung, Microchannel anechoic Corner for size-selective separation and medium Exchange via traveling surface acoustic waves, Anal. Chem. 87 (9) (2015) 4627–4632.
- [31] G. Destgeer, H.J. Sung, Recent advances in microfluidic actuation and micro-object manipulation via surface acoustic waves, Lab Chip 15 (13) (2015) 2722–2738.
- [32] S.M. Majd, A. Salimi, B. Astinchap, Label-free attomolar detection of lactate based on radio frequency sputtered of nickel oxide thin film field effect transistor, Biosens. Bioelectron. 92 (2017) 733–740.
- [33] M.A. Cooper, Label-free screening of bio-molecular interactions, Anal. Bioanal.

- Chem. 377 (5) (2003) 834-842.
- [34] S. Chatterjee, S.A. Bryan, C.J. Seliskar, W.R. Heineman, Three-component spectroelectrochemical sensor module for the detection of pertechnetate (TcO4-), Rev. Anal. Chem. 32 (3) (2013) 209–224.
- [35] S. Chatterjee, A.S. Del Negro, M.K. Edwards, S.A. Bryan, N. Kaval, N. Pantelic, L.K. Morris, W.R. Heineman, C.J. Seliskar, Luminescence-based spectro-electrochemical sensor for [Trc(dmpe)(3)](2+/+) (dmpe=1,2-bis(dimethylphosphino)ethane) within a charge-selective polymer film, Anal. Chem. 83 (5) (2011) 1766–1772
- [36] S. Chatterjee, A.E. Norton, M.K. Edwards, J.M. Peterson, S.D. Taylor, S.A. Bryan, A. Andersen, N. Govind, T.E. Albrecht-Schmitt, W.B. Connick, T.G. Levitskaia, Highly selective colorimetric and luminescence response of a square-planar platinum(II) terpyridyl complex to aqueous TcO4-, Inorg. Chem. 54 (20) (2015) 9914–9923.
- [37] N. Kaval, C.J. Seliskar, W.R. Heineman, Spectroelectrochemical sensing based on multimode selectivity simultaneously achievable in a single device. 16. Sensing by fluorescence, Anal. Chem. 75 (22) (2003) 6334–6340.
- [38] J.M. Gong, T. Fang, D.H. Peng, A.M. Li, L.Z. Zhang, A highly sensitive photoelectrochemical detection of perfluorooctanic acid with molecularly imprined polymer-functionalized nanoarchitectured hybrid of AgI-BiOI composite, Biosens. Bioelectron. 73 (2015) 256–263.
- [39] T.T. Tran, J.Z. Li, H. Feng, J. Cai, L.J. Yuan, N.Y. Wang, Q.Y. Cai, Molecularly imprinted polymer modified TiO2 nanotube arrays for photoelectrochemical determination of perfluorooctane sulfonate (PFOS), Sens. Actuators B-Chem. 190 (2014) 745–751.
- [40] W.W. Zhao, M. Xiong, X.R. Li, J.J. Xu, H.Y. Chen, Photoelectrochemical bioanalysis: A mini review, Electrochem. Commun. 38 (2014) 40–43.
- [41] J.A. Cooper, M. Wu, R.G. Compton, Photoelectrochemical analysis of ascorbic acid, Anal. Chem. 70 (14) (1998) 2922–2927.
- [42] Q. Kang, L.X. Yang, Y.F. Chen, S.L. Luo, L.F. Wen, Q.Y. Cai, S.Z. Yao, Photoelectrochemical detection of pentachlorophenol with a multiple hybrid CdSexTe1-x/TiO2 nanotube structure-based label-Free immunosensor, Anal. Chem. 82 (23) (2010) 9749–9754.
- [43] Z.Q. Yang, F.R. Wang, M. Wang, H.S. Yin, S.Y. Ai, A novel signal-on strategy for M.SssI methyltransfease activity analysis and inhibitor screening based on photoelectrochemical immunosensor, Biosens. Bioelectron. 66 (2015) 109–114.
- [44] M.M. Liang, S.L. Liu, M.Y. Wei, L.H. Guo, Photoelectrochemical oxidation of DNA by ruthenium tris(bipyridine) on a tin oxide nanoparticle electrode, Anal. Chem. 78 (2) (2006) 621–623.
- [45] N. Haddour, S. Cosnier, C. Gondran, Electrogeneration of a biotinylated poly(pyr-role-ruthenium(II)) film for the construction of photoelectrochemical immunosensor, Chem. Commun. 21 (2004) 2472–2473.
- [46] B. Sun, F.M. Qiao, L.J. Chen, Z. Zhao, H.S. Yin, S.Y. Ai, Effective signal-on photoelectrochemical immunoassay of subgroup J avian leukosis virus based on Bi2S3 nanorods as photosensitizer and in situ generated ascorbic acid for electron donating, Biosens, Bioelectron. 54 (2014) 237–243.
- [47] K. Chen, M.C. Liu, G.H. Zhao, H.J. Shi, L.F. Fan, S.C. Zhao, Fabrication of a novel and simple microcystin-LR photoelectrochemical sensor with High sensitivity and selectivity, Environ. Sci. Technol. 46 (21) (2012) 11955–11961.
- [48] B.J. Lu, M.C. Liu, H.J. Shi, X.F. Huang, G.H. Zhao, A novel photoelectrochemical sensor for bisphenol A with High sensitivity and selectivity based on surface molecularly imprinted polypyrrole modified TiO2 nanotubes, Electroanalysis 25 (3) (2013) 771–779.
- [49] J.M. Gong, X.Q. Wang, X. Li, K.W. Wang, Highly sensitive visible light activated photoelectrochemical biosensing of organophosphate pesticide using biofunctional crossed bismuth oxyiodide flake arrays, Biosens. Bioelectron. 38 (1) (2012) 43–49.
- [50] C.A. Schroll, S. Chatterjee, W.R. Heineman, S.A. Bryan, Thin-layer spectroelectrochemistry on an aqueous microdrop, Electroanalysis 24 (5) (2012) 1065–1070.
- [51] R.W. Murray, W.R. Heineman, G.W. Odom, An optically transparent thin layer electrochemical cell, Anal. Chem. 39 (13) (1967) 1666-&.
- [52] C.A. Schroll, S. Chatterjee, T.G. Levitskaia, W.R. Heineman, S.A. Bryan, Electrochemistry of europium(III) chloride in 3 LiCl - NaCl, 3 LiCl-2 KCl, LiCl - RbCl, and 3 LiCl-2 CsCl eutectics at various temperatures, J Electrochem. Soc. 164 (8) (2017) H5345–H5352.
- [53] C.A. Schroll, S. Chatterjee, T. Levitskaia, W.R. Heineman, S.A. Bryan, Spectroelectrochemistry of EuCl3 in Four molten Salt eutectics; 3 LiCl-NaCl, 3 LiCl-2 KCl, LiCl-RbCl, and 3 LiCl-2 CsCl; At 873 K, Electroanalysis 28 (9) (2016) 2158–2165.
- [54] C.A. Schroll, S. Chatterjee, T.G. Levitskaia, W.R. Heineman, S.A. Bryan, Electrochemistry and spectroelectrochemistry of europium(III) chloride in 3LiCl-2KCl from 643 to 1123 K, Anal. Chem. 85 (20) (2013) 9924–9931.
- [55] J.E. Pander, M.F. Baruch, A.B. Bocarsly, Probing the mechanism of aqueous CO2 reduction on Post-transition-metal electrodes using ATR-IR spectroelectrochemistry, Acs Catal. 6 (11) (2016) 7824–7833.
- [56] T. Tachikawa, T. Ochi, Y. Kobori, Crystal-face-dependent charge dynamics on a BiVO4 photocatalyst revealed by single-particle spectroelectrochemistry, ACS Catal. 6 (4) (2016) 2250–2256.
- [57] S. Enengl, C. Enengl, P. Stadler, H. Neugebauer, N.S. Sariciftci, Spectroelectrochemical studies on quinacridone by using poly(vinyl alcohol) coating as protection layer, Chemphyschem 16 (10) (2015) 2206–2210.
- [58] H.E. Toma, K. Araki, Spectroelectrochemical characterization of organic and metalorganic compounds, Curr. Org. Chem. 6 (1) (2002) 21–34.
- [59] I. Schmidt, A. Pieper, H. Wichmann, B. Bunk, K. Huber, J. Overmann, P.J. Walla, U. Schroder, In situ autofluorescence spectroelectrochemistry for the study of microbial extracellular electron transfer, ChemCatChem 4 (10) (2017) 2515–2519.

- [60] S. Chatterjee, S.A. Bryan, A.J. Casella, J.M. Peterson, T.G. Levitskaia, Mechanisms of neptunium redox reactions in nitric acid solutions, Inorg. Chem. Front. 4 (4) (2017) 581–594.
- [61] S.D. Branch, A.D. French, A.M. Lines, C.Z. Soderquist, B.M. Rapko, W.R. Heineman, S.A. Bryan, In situ spectroscopic analysis and quantification of [Tc(CO)(3)](+) in hanford tank waste, Environ. Sci. Technol. 52 (14) (2018) 7796–7804.
- [62] E. Arunkumar, A. Ajayaghosh, J. Daub, Selective calcium ion sensing with a bichromophoric squaraine foldamer, J. Am. Chem. Soc. 127 (9) (2005) 3156–3164.
- [63] A.K. Singh, S. Mehtab, Calcium(II)-selective potentiometric sensor based on atfurildioxime as neutral carrier, Sens. Actuators B-Chem. 123 (1) (2007) 429–436.
- [64] H. Durr, G. Dorr, K. Zengerle, J.M. Curchod, A.M. Braun, On the mechanism of the photoreduction of Water with ruthenium-trisbipyrazil as sensitizer, Helv. Chim. Acta 66 (8) (1983) 2652–2655.
- [65] K. Kalyanasundaram, Photophysics, photochemistry and solar-energy conversion with tris(bipyridyl)ruthenium(Ii) and its analogs, Coordin Chem. Rev. 46 (October) (1982) 159–244.
- [66] C.A. Schroll, S. Chatterjee, W.R. Heineman, S.A. Bryan, Semi-infinite linear diffusion spectroelectrochemistry on an aqueous micro-drop, Anal. Chem. 83 (11) (2011) 4214–4219.
- [67] S. Chatterjee, A.S. Del Negro, F.N. Smith, Z.M. Wang, S.E. Hightower, B.P. Sullivan, W.R. Heineman, C.J. Seliskar, S.A. Bryan, Photophysics and luminescence spectroelectrochemistry of [Tc(dmpe)(3)](+/2+) (dmpe=1,2-bis(dimethylphosphino) ethane), J Phys. Chem. A 117 (48) (2013) 12749–12758.
- [68] M.N. Szentirmay, C.R. Martin, Ion-Exchange selectivity of nafion films on electrode surfaces, Anal. Chem. 56 (11) (1984) 1898–1902.
- [69] A.N. Khramov, M.M. Collinson, Electrogenerated chemiluminescence of tris(2,2'-bipyridyl)ruthenium(II) ion-exchanged in nafion-silica composite films, Anal. Chem. 72 (13) (2000) 2943–2948.
- [70] T.M. Downey, T.A. Nieman, Chemiluminescence detection using regenerable tris (2,2'-bipyridyl)ruthenium(li) immobilized in nafion, Anal. Chem. 64 (3) (1992) 261–268.
- [71] I. Zudans, J.R. Paddock, H. Kuramitz, A.T. Maghasi, C.M. Wansapura, S.D. Conklin, N. Kaval, T. Shtoyko, D.J. Monk, S.A. Bryan, T.L. Hubler, J.N. Richardson, C.J. Seliskar, W.R. Heineman, Electrochemical and optical evaluation of noble metal- and carbon-ITO hybrid optically transparent electrodes, J. Electroanal. Chem. 565 (2) (2004) 311–320.
- [72] Fleteison, J., Ion Exchange. Marcel Dekker: New York, 1969; Vol. 2.
- [73] A. Schwarz, G.E. Boyd, Thermodynamics of Exchange of tetramethylammonium with sodium ions in Cross-linked polystyrene sulfonates at 25 degrees, J. Phys. Chem.-Us 69 (12) (1965) 4268-&.
- [74] I. Zudans, W.R. Heineman, C.J. Seliskar, In situ measurements of chemical sensor film dynamics by spectroscopic ellipsometry. Partitioning of a chromophore, J Phys. Chem. B 108 (31) (2004) 11521–11528.
- [75] P.T. Kissinger, W.R. Heineman, Cyclic voltammetry, J Chem. Educ. 60 (9) (1983) 702–706.
- [76] N. Pantelic, C.M. Wansapura, W.R. Heineman, C.J. Seliskar, Dynamic in situ spectroscopic ellipsometry of the reaction of aqueous iron(II) with 2,2'-bipyridine in a thin nafion film, J Phys. Chem. B 109 (29) (2005) 13971–13979.
- [77] C.A. Schneider, W.S. Rasband, K.W. Eliceiri, NIH image to imageJ: 25 years of image analysis, Nat. Methods 9 (7) (2012) 671–675.
- [78] J. Schindelin, I. Arganda-Carreras, E. Frise, V. Kaynig, M. Longair, T. Pietzsch,

- S. Preibisch, C. Rueden, S. Saalfeld, B. Schmid, J.Y. Tinevez, D.J. White, V. Hartenstein, K. Eliceiri, P. Tomancak, A. Cardona, Fiji: an open-source platform for biological-image analysis, Nat. Methods 9 (7) (2012) 676–682.
- [79] L.K. Morris, E.A. Abu, C. Bowman, C.E. Estridge, S.E. Andria, C.J. Seliskar, W.R. Heineman, Effect of the concentration of supporting electrolyte on spectroelectrochemical detection of [Ru(bpy)<sub>(3)</sub>]<sup>(2+)</sup>, Electroanalysis 23 (4) (2011) 939–946
- [80] P. Bertoncello, L. Dennany, R.J. Forster, P.R. Unwin, Nafion tris(2-2'-bipyridyl) ruthenium(II) ultrathin Langmuir Schaefer films: redox catalysis and electro-chemiluminescent properties, Anal. Chem. 79 (19) (2007) 7549–7553.
- [81] P. Bertoncello, I. Ciani, D. Marenduzzo, P.R. Unwin, Kinetics of solute partitioning into ultrathin nafion films on electrode surfaces: theory and experimental measurement, J. Phys. Chem. C 111 (1) (2007) 294–302.
- [82] M.A. Edwards, P. Bertoncello, P.R. Unwin, Slow diffusion reveals the intrinsic electrochemical activity of basal plane highly oriented pyrolytic graphite electrodes, J. Phys. Chem. C 113 (21) (2009) 9218–9223.
- [83] W.R. Heineman, P.T. Kissinger, Laboratory Techniques in Electroanalytical Chemistry, Marcell Dekker, New York, 1996.
- [84] P. Bertoncello, I. Ciani, F. Li, P.R. Unwin, Measurement of apparent diffusion coefficients within ultrathin nafion Langmuir-Schaefer films: comparison of a novel scanning electrochemical microscopy approach with cyclic voltammetry, Langmuir 22 (25) (2006) 10380–10388.
- [85] G.L. Long, J.D. Winefordner, Limit of detection, Anal. Chem. 55 (7) (1983) A712-+.
- [86] N. Formisano, P. Jolly, N. Bhalla, M. Cromhout, S.P. Flanagan, R. Fogel, J.L. Limson, P. Estrela, Optimisation of an electrochemical impedance spectroscopy aptasensor by exploiting quartz crystal microbalance with dissipation signals, Sens. Actuators B: Chem. 220 (2015) 369–375.
- [87] N. Mavrogiannis, X. Fu, M. Desmond, R. McLarnon, Z.R. Gagnon, Monitoring microfluidic interfacial flows using impedance spectroscopy, Sens. Actuators B: Chem. 239 (2017) 218–225.
- [88] S. Basuray, S. Senapati, A. Aijian, A.R. Mahon, H.C. Chang, Shear and AC Field enhanced carbon nanotube impedance assay for Rapid, sensitive, and mismatchdiscriminating DNA hybridization, ACS Nano 3 (7) (2009) 1823–1830.
- [89] J. Zheng, R.S. Vemuri, L. Estevez, P.K. Koech, D.M. Camaioni, B.P. McGrail, R.K. Motkuri, Pore engineering of metal-organic frameworks for adsorption cooling applications, J. Am. Chem. Soc. 139 (31) (2018) 10601–10604.
- [90] R.K. Motkuri, H.V.R. Annapureddy, V. Murugesan, B.P. McGrail, X. Li. Dang, R. Krishna, P.K. Thallapally, Fluorocarbon adsorption in hierarchical porous frameworks, Nat. Commun. 5 (2014) 4368.

Sayandev Chatterjee graduated in September 2009 from the University of Cincinnati with a pH.D. in Chemistry and joined PNNL in 2009 as a post-doctoral researcher in the Energy and Environment Directorate in 2009, and was hired as a staff in 2013. His research interests include porous materials, electrochemistry and chemical and electrochemical sensors. He has, over the last few years, worked extensively on strategies for environmental sensing, and have successfully designed highly sensitive chemical sensors for various anionic contaminants (pertechnetate and nitrate) as well as electrochemical sensors for detecting haloalkanes in water. He has one patent titled "Method and apparatus for simultaneous spectroelectrochemical analysis."